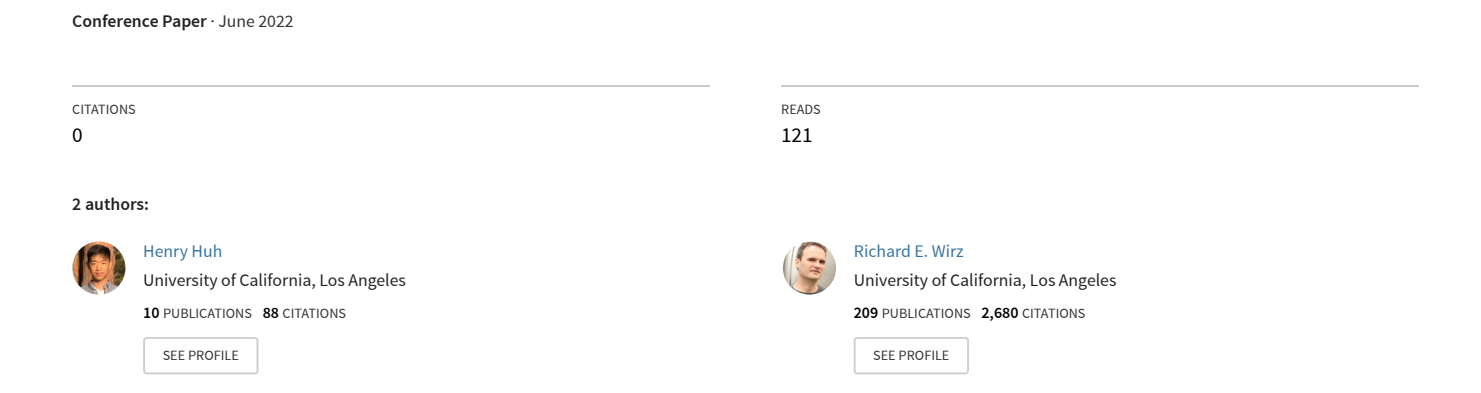
Numerical Simulation of Cone-Jet and Emission Processes for Electrospray Thrusters



Numerical Simulation of Cone-Jet and Emission Processes for Electrospray Thrusters

IEPC-2022-211

Presented at the 37th International Electric Propulsion Conference Massachusetts Institute of Technology, Cambridge, MA, USA June 19-23. 2022

Henry Huh¹ and Richard E. Wirz ² *University of California, Los Angeles, CA, 90095, USA*

The leaky-dielectric model is incorporated in the Finite Volume Method (FVM) code, OpenFOAM, to investigate the electrospray emission behavior of low to moderate conductivity liquids. Compared to previous studies, this is the first Finite Volume Method (FVM) based model for higher conductivity liquid accurately predicting the cone-jet formation and droplet breakup. This was possible by incorporating a novel interface interpolation devised to conserve the charge for higher conductivity liquid. The model is validated against experimental data for heptane and tributyl phosphate and scaling relationships for diameter and specific charge of emitted droplets. The results reveal the behavior of low and moderate conductivity liquids with respect to key operating conditions, i.e., flow rate, voltage, and fluid properties, i.e., surface tension, and viscosity. The parametric evaluations reveal important emission metrics closely related to the meniscus shape and charge distribution along the cone-jet. Decreasing non-dimensional flow rate or increasing Electric Reynolds number leads to the emergence of convex-upward meniscus of the cone allowing high charge concentration at the cone-to-jet region. High charge concentration with shortened cone-to-jet length ultimately results in increased specific charge of emitted droplet with increased jetting velocity which are important electrospray metrics.

I. Introduction

A conical meniscus is developed by surface tension and electrostatic forces balanced on the interface in the cone-jet mode. Zeleny *et al.* [1] first observed different modes of electrosprays including the steady cone-jet mode, which has been of significant interest for stable emission of droplets. Cloupeau *et al.*[2] examined various cone-jet structures and operating modes experimentally in a range of operating conditions and physical properties of low to moderate conductivity liquids $(2 \times 10^{-8} \text{ S m}^{-1} \text{ to } 1 \times 10^{-4} \text{ S m}^{-1})$. Taylor and Ingram [3] applied electrostatic analysis for perfectly conductive liquid up to the location where a jet begins to develop from the cone; the half-angle at the apex of the cone was shown to be 49.3°. The Ohmic, leaky-dielectric model of Melcher and Taylor [4] supplements Taylor's analysis by introducing tangential electrostatic force due to free charge accumulation at the liquid interface, unlike in perfect conductors and dielectrics involving perpendicular electrical stresses. Pantano *et al.* [5] solved the zeroth-order electrostatic equations from the theory of [3] to observe the effect of charge accumulation effect on cone-jet formation. They acquired the meniscus shape with a conical tip for the first time assuming the vertex angle as 49.3°. The charge accumulation at the tip of the meniscus allows high enough electrostatic force dominating over the surface tension force in the cone-to-jet region. Furthermore, a concave-upward meniscus transitions to a convex meniscus with decreasing Taylor's number, $\frac{\varepsilon_0 \phi_0^2}{2\gamma R_e}$ where ε_0 , ϕ_0 , γ , and R_e are respectively vacuum permittivity, potential relative to the ground electrode, surface tension and outer diameter of the electrode ([5]).

Important scaling relationships have been developed to correlate the output parameters of interest under different assumptions ([6–8]). Although they provide valuable physical insights, the scaling laws cannot describe the emission mechanics during evolution of a cone-jet and subsequent droplet breakup. Several numerical models have been

¹Ph.D. student, Mechanical and Aerospace Engineering, henryhuh89@g.ucla.edu

²Professor, Mechanical and Aerospace Engineering, wirz@ucla.edu

developed to describe the processes of cone-jet formation and electrospray emission. The boundary element/integral method (BEM) ([5, 9, 10]) is computationally cost-efficient and allows accurate analysis under the given constraints. Higuera [9] investigated the surface charge density with varying flow rates and permittivities with the far-field boundary conditions obtained from electrostatic solution ([3]) in a restricted cone-to-jet region. Gamero-Castaño [10] went further to obtain solution in an extended cone-to-jet region, concluding that the surface position of TBP largely invariant to physical properties and flow rates for dielectric constants of 8.91 and 64.9. The BEM is restricted to a linear problem of a single dimension along the interface, which does not allow prediction of emitted droplets or internal flow in bulk liquid, which are important observable parameters in electric propulsion.

The finite volume method (FVM) allows robust handling of nonlinear conservation equations as a more flexible approach than the BEM. The FVM can reproduce not only the cone-jet structure but also downstream breakup and emitted droplets in an electrospray ([11, 12]). Several EHD models have been developed on the basis of the FVM. López-Herrera *et al.* and Herrada *et al.* [13, 14] used the Volume-of-Fluid method to track interfaces in a multiphase problem by an open-source tool, Gerris ([15]). Roghair *et al.* [11] developed an EHD OpenFOAM code based on the work of [13], which was extended by Dastourani *et al.* [12] to simulate electrosprays of low conductivity ($\sim 1 \times 10^{-8}$ S m⁻¹ to $\sim 1 \times 10^{-6}$ S m⁻¹) liquid. Previous research based on the FVM has been focused on low conductivity liquids ($\sim 1 \times 10^{-8}$ S m⁻¹) ([11–14, 16]. Modeling electrosprays of moderate to high conductivity ($\sim 1 \times 10^{-5}$ S m⁻¹ to $\sim 1 \times 10^{-2}$ S m⁻¹) requires additional numerical treatment to accurately resolve jet breakup and droplet formation.

The objective herein is to develop a high-fidelity EHD model that can provide detailed emission mechanisms for electrospray devices in a wide range of operating conditions and fluid properties. In this work we will validate the suggested models against experimental observations and scaling relationships for low ($\sim 1 \times 10^{-7} \, \mathrm{S} \, \mathrm{m}^{-1}$) and moderate conductivity ($\sim 1 \times 10^{-4} \, \mathrm{S} \, \mathrm{m}^{-1}$) liquids. In particular, we run the model across the operating conditions and the fluid properties critical in defining the steady cone-jet mode. We will show how the charge distribution varies along the interface and how the meniscus shape is determined by the competing electrostatic and surface tension forces on the interface. The governing equations are discussed in Section II and numerical methods in Section III. The modeling results for the low conductivity ($\sim 1 \times 10^{-7} \, \mathrm{S} \, \mathrm{m}^{-1}$) liquid are presented in Section IV.A and the moderate conductivity ($\sim 1 \times 10^{-4} \, \mathrm{S} \, \mathrm{m}^{-1}$) liquid in Section IV.B. The concluding remarks are provided in Section V.

II. Model Formulation

A. Fluid flow

Electrohydrodynamic fluid flow is governed by the incompressible continuity and momentum equations given as,

$$\mathbf{u} = 0,\tag{1}$$

$$\rho \left[\frac{\partial \mathbf{u}}{\partial t} + \mathbf{u} \mathbf{u} \right] = -\mathbf{P} + \mu^2 \mathbf{u} + \rho \mathbf{g} + \mathbf{F}_E + \mathbf{F}_{ST}, \tag{2}$$

where u, t, ρ , P, and μ represent respectively velocity, time, density, pressure, and dynamic viscosity. Note the electrostatic force, F_E , and the surface tension force, F_{ST} , added to the momentum equation ([13]). Here F_{ST} is given as

$$\mathbf{F}_{ST} = \gamma \kappa \alpha = \gamma(-\hat{\mathbf{n}})\alpha,\tag{3}$$

$$\hat{\boldsymbol{n}} = \frac{\alpha}{|\alpha| + \delta'},\tag{4}$$

where the surface tension term is reformulated according to the continuum surface force (CSF) model by [17]. γ is the surface tension coefficient, κ is the interface curvature and \hat{n} is the unit normal vector. δ' is a small number relative to $|\alpha|$ to ensure a non-zero denominator in Eq. 4.

The Volume-Of-Fluid (VOF) method ([18]) captures the interface between liquid and vacuum by using a Heaviside function of the liquid volume fraction, α_{liq} . Each computational cell is represented as $\alpha_{liq}=0$ within a gas or vacuum, $\alpha_{liq}=1$ within the liquid and $0<\alpha_{liq}<1$ at the interface. The liquid volume fraction is calculated by solving the transport equation given as

$$\frac{\partial \alpha_{liq}}{\partial t} + (\boldsymbol{u}\alpha_{liq}) + (\alpha_{liq}(1 - liq)\boldsymbol{u_r}) = 0, \tag{5}$$

$$u_r = C_{alpha} \left| \frac{\phi_a}{|S_a|} \right| \hat{n}, \tag{6}$$

where u_r is an artificial compression term for sharpness of the interface ([19]). ϕ_a , S_a , and C_{alpha} are velocity flux, face surface area and an adjustable compression factor. C_{alpha} is set to unity here, whereas it is between 0 to 4 in most practical cases. Large C_{alpha} allows a sharp interface, but increases the magnitude of spurious current ([20, 21]). In the conventional VOF method a cell-averaged property, ψ , such as density, viscosity, electrical conductivity or permittivity is calculated as

$$\psi = \psi_1 \alpha_{liq} + \psi_2 (1 - \alpha_{liq}) (\psi \in [\rho, \nu, \sigma, \varepsilon])$$
(7)

where ψ_1 and ψ_2 are the properties in liquid and vacuum respectively. The interface is reconstructed from the liquid volume fraction, α_{liq} , and the solution of transport equations for all relevant cell-averaged properties.

B. Electrostatics

The volumetric electrostatic force, F_E , is described by the Maxwell's equations which are reduced to the electrostatic equation with negligible magnetic effect in Eq. 8. The Gauss's law is given in Eq. 9 as

$$\times E = 0; \tag{8}$$

$$(\varepsilon \mathbf{E}) = \rho_e, \tag{9}$$

where E is the electric field vector, ε is the electrical permittivity and ρ_e is the volumetric charge density.

$$\frac{\partial \rho_e}{\partial t} + \boldsymbol{J} = 0,\tag{10}$$

The charge conservation equation in Eq. 10 is converted to Eq. 11 by substituting the current density, J, as the sum of Ohmic conduction and charge convection as $J = \sigma E + \rho_e u$,

$$\frac{\partial \rho_e}{\partial t} + (\rho_e \mathbf{u}) = -(\sigma \mathbf{E}). \tag{11}$$

The electrostatic force is given as the sum of Coulombic and polarization forces as

$$F_E = \rho_e E - \frac{1}{2} E^2 \varepsilon, \tag{12}$$

which acts on the electric charge accumulated on the surface of an electrospray. The non-dimensional flow rate, δ , is defined in Eq. 13, and the electric Reynolds number, Re_E , in Eq. 14 where Q is the flow rate, and ε_0 is the vacuum permittivity.

$$\delta = \frac{\rho \sigma Q}{\gamma \varepsilon_0},\tag{13}$$

$$Re_E = \left(\frac{\rho \varepsilon_0 \gamma^2}{\mu^3 \sigma}\right)^{\frac{1}{3}}.$$
 (14)

III. Numerical Methods

The open-source code OpenFOAM ([22]) is based on the FVM to obtain linearized relationships among neighboring cell-averaged variables of the governing equations. The 2^{nd} -order-accurate linear upwind scheme ([23, 24]) is employed to suppress false diffusion due to the discretized convection term. As the velocity boundary condition, a fixed uniform value is applied as the velocity boundary condition at the inlet, the zero-gradient condition at the outlet and the wall, the symmetry condition on the axis and the cyclic boundary condition at the front and the back for the wedge-shaped

three-dimensional domain. Similarly, for the pressure boundary condition, the zero-gradient is applied at the inlet and zero total pressure at the outlet and on the wall to maintain vacuum in the domain. sensitivity study is performed to determine to the total number of mesh cells, N_c , large enough to show no further dependence of the computed results on the grid size. N_c is set equal to 138, 800 for the low conductivity case and 98, 990 for the moderate conductivity case, where the droplet diameter converges to 15.6 μ m for heptane of low conductivity and 6 μ m for TBP of moderate conductivity respectively.

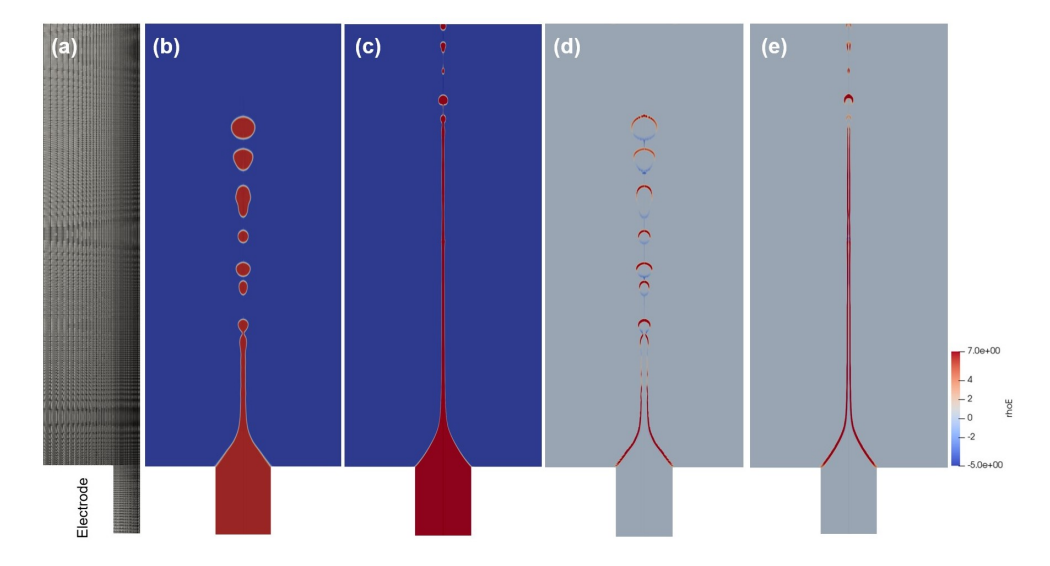


Fig. 1 Comparison of WAM and the new interpolation scheme for heptane, (a) computational domain, (b) liquid volume fraction for f = 1(WAM), (c) liquid volume fraction of f = 20, (d) charge density for f = 1, and (e) charge density for f = 20

The VOF method ([25, 26]) is employed to reconstruct the interface to capture the interfacial forces on the jet and the cone meniscus between liquid and vacuum. Preliminary results showed the importance of avoiding false leakage of mass and charge through appropriate treatment of the cell-averaged quantities at the liquid-vacuum interface. Tomar *et al.* and López-Herrera *et al.* [13, 27] used the weighted arithmetic mean (WAM) for two-phase σ and ε based on their linear weighted average in terms of the liquid volume fraction. In our simulation WAM leads to significant numerical diffusion with no droplet breakup occurring for moderate to high conductivity liquids. López-Herrera *et al.* [13] investigated the interpolation schemes, weighted arithmetic mean (WAM) and weighted harmonic mean (WHM), concluding that the WHM does not provide any better accuracy for moderately-conductive dielectric-conducting liquid. The WHM essentially assigns zero conductivity to all cells involving any liquid-vacuum interface to result in code failure due to abrupt change in the physical properties between neighboring cells. In this study we applied a new interpolation scheme in Eq. 15 and Eq. 16 to determine the cell-averaged conductivity and permittivity in every two-phase cell involving the interface. Note that Eq. 15 and Eq. 16 reduce to the WAM for f = 1 and the WHM for f = -1.

$$\sigma_{cell} = \left(\alpha_{liq}\sigma_{liq}^{1/f} + (1 - \alpha_{liq})\sigma_{vac}^{1/f}\right)^f,\tag{15}$$

$$\varepsilon_{cell} = \left(\alpha_{liq}\varepsilon_{liq}^{1/f} + (1 - \alpha_{liq})\varepsilon_{vac}^{1/f}\right)^f. \tag{16}$$

 σ_{cell} and ε_{cell} are the cell averaged quantities and α_{liq} is the liquid volume fraction. The subscripts, liq and vac, represent liquid and vacuum respectively. σ_{vac} is equal to zero and ε_{vac} is equal to the vacuum permittivity, ε_0 . The liquid volume fraction and the corresponding charge density are shown for f=1(WAM) and f=20 in Figure 1. Linear interpolation for the f=1(WAM) results in smoothly varying σ and ε with significant false leakage and diffusion occurring through the interface. Note the erroneous results by the WAM showing excessive droplet sizes and failure in charge conservation for heptane in Figure 1. Note that charge is well conserved to result in converged droplet diameters showing no further dependence on f for f>20. It is a compromise between smooth resolution without code failure and a sharp interface with suppressed numerical diffusion. A larger f better reproduces sharp variation of σ and ε with

less false diffusion leading to a finer jet and smaller droplets. The maximum charge density is ρ_E , $max = 430 \,\text{C/m}^2$ for f = 20 and ρ_E , $max = 60 \,\text{C/m}^2$ for f = 1 in Figure 1. Obviously finer grids will be required for better resolution accuracy and numerical stability for electrosprays of high conductivity liquids.

IV. Results and Discussion

The computational domain covers the region from emitter to extractor both in [16] (Section IV.A) and [28] (Section IV.B). Simulation is based on the published experimental setups with the given physical properties and operating conditions including flow rate and voltage. Photographs in [16] show the experimentally observed cone-jet formation and emitted droplets for heptane of low conductivity. Relevant physical properties are listed for heptane of low conductivity and TBP of moderate conductivity in Table 1.

The total current, *I*, in an electrospray includes the two contributions by charge conduction in Eq. 17 and by charge convection in Eq. 18 given as

$$I_d(z) = 2\pi\sigma \int_0^{r_s} E_z r \, \mathrm{d}r,\tag{17}$$

$$I_s(z) = 2\pi q_s v_s r_s,\tag{18}$$

where r is the radial coordinate, r_s is the radius of the cone-jet, v_s is the liquid velocity, q_s is the surface charge density and E_z is the longitudinal component of the electric field vector. We define the cone-to-jet length, L_{cj} , as the region where the convective current changes from 5 % to 95 % of its final value. It corresponds to the transition region in [10] and the charge relaxation region in [8]. The charge relaxation time is defined as $\tau_e = \frac{\varepsilon}{\sigma}$.

Table 1 Liquid properties of heptane and tributyl phosphate (TBP)

Liquid	$\rho(kg/m^3)$	$\sigma(S/m)$	$\gamma(N/m)$	$\varepsilon(F/m)$	$\mu(PaS)$
Heptane	684	6.26×10^{-7}	0.0186	1.91	4.28×10^{-4}
TBP	976	2.3×10^{-4}	0.028	8.91	3.59×10^{-3}

A. Low conductivity

Figure 2(a,b) shows the computational domain and grid for the experimental setup in [16]. The nozzle and outer diameters are $120 \,\mu m$ and $450 \,\mu m$, the orifice diameter is $12 \,m m$ and the distance between emitter and extractor is 29.8 mm. Figure 2(c,d) show the computed distributions of liquid volume fraction and contour and magnitude of the electric field on a 2-D plane through the axis. Note the maximum electric field at the cone-to-jet region well below the minimum threshold for ion emission ($\sim 1 \times 10^9 \, V \, m^{-1}$) ([29]). Scaling relationships are given for the non-dimensional droplet diameter and the total current, respectively in Eq. 19 and Eq. 20 ([6]). Another scaling law is given for the non-dimensional droplet diameter in Eq. 21 ([8]). ε_r is the relative permittivity in Eq. 21.

$$D = \left(\frac{\rho \varepsilon_0 Q^3}{\sigma \gamma}\right)^{\frac{1}{6}},\tag{19}$$

$$I = (\gamma \sigma Q)^{\frac{1}{2}}, \tag{20}$$

and

$$D = \left(\frac{\varepsilon_r \varepsilon_0 Q}{\sigma}\right)^{\frac{1}{3}}.$$
 (21)

 D^* in Figure 3 and 6 represents the mean droplet diameter normalized by the inner diameter of the emitter. In Figure 3(a) $1/Re_E$ ranges from 0.03 to 0.068 for the non-dimensional flow rate varying from $\delta = 2.4$ to $\delta = 9.7$. In Figure 3(b) the voltage is varied from 3 kV to 5 kV for the non-dimensional flow rates of 13.9, 46.4, and 69.6 according to [16]. Reasonable agreement is shown with proper trends of variation of D^* for model predictions, scaling laws and

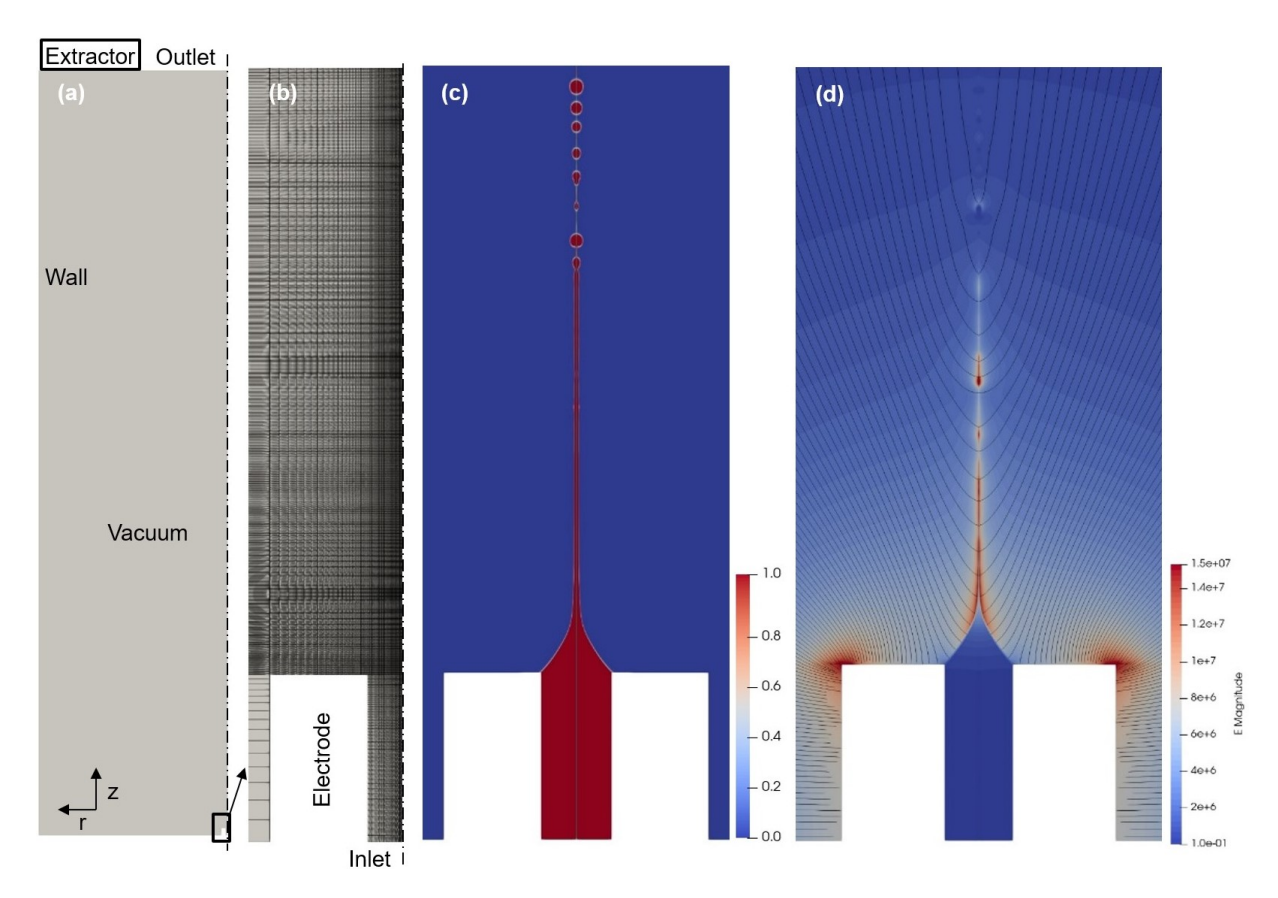


Fig. 2 Computation for heptane of low conductivity liquid in steady cone-jet operation; (a) axisymmetric domain with 138,800 cells, (b) magnified emission region, (c) liquid volume fraction and (d) magnitude and contour of the electric field

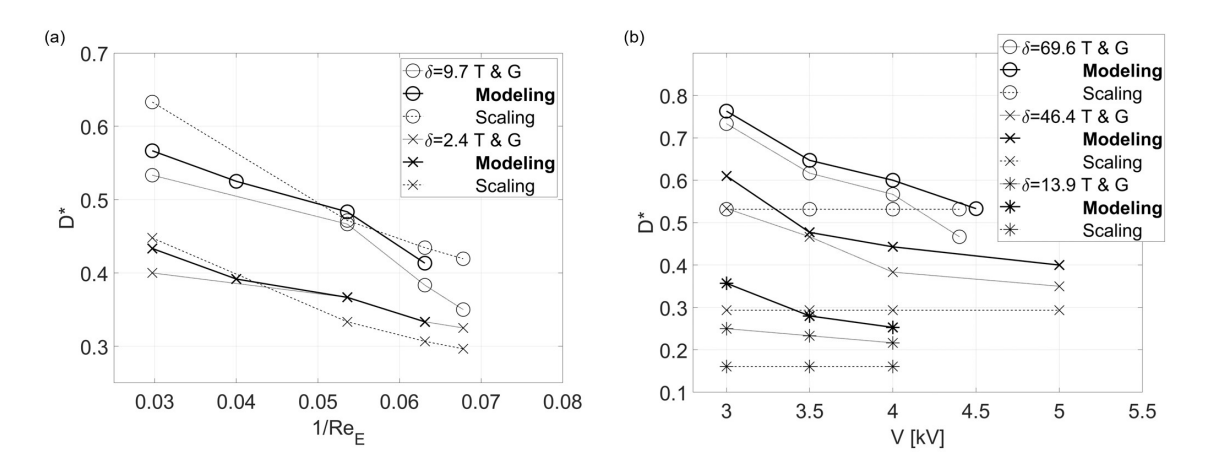


Fig. 3 Comparison of non-dimensional droplet diameters, D^* , by experiment (T & G, [16]), modeling and scaling ([6]) for heptane at different δ 's with respect to (a) $1/Re_E$ and (b) voltage

experimental observations in Figure 3. The mean droplet diameter in the steady cone-jet mode is compared with the universal scaling law in Eq. 19 and the experimental results in [16]. The droplet size was reported to decrease with decreasing Re_E , decreasing flow rate and increasing voltage as previously discussed in literature ([6–8, 12, 16, 28]). Although Eq. 19 and Eq. 21 are given as functions of flow rate and physical properties only, the measured and computed

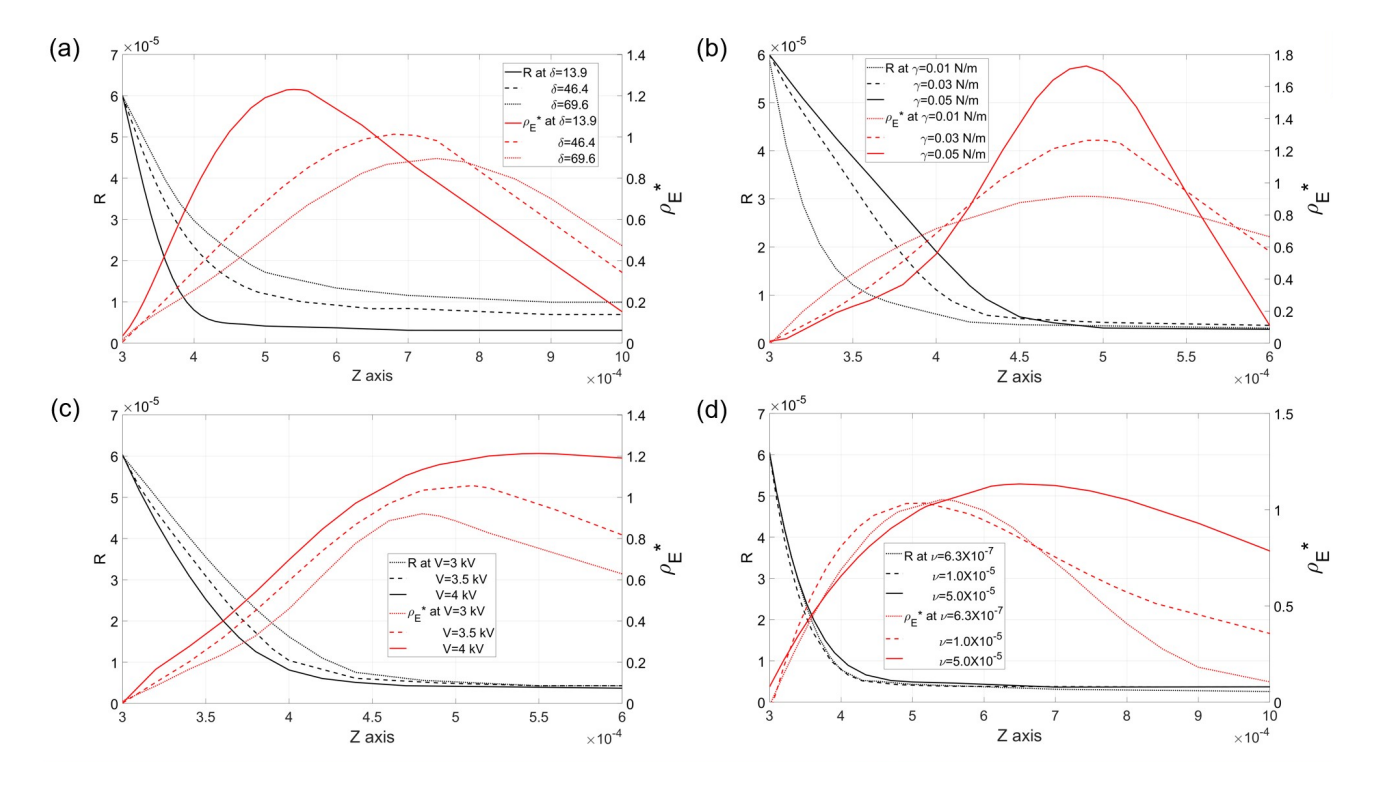


Fig. 4 Predicted distributions of radius and charge density distribution along the meniscus for heptane at different (a) dimensionless flow rate δ , (b) surface tension coefficient, γ [N m⁻¹], (c) voltage, V [kV], (d) kinematic viscosity, ν (= μ/ρ) [Pa s], (e) relative permittivity, ε_r

droplet diameters show strong dependence on the voltage with the increasing flow rate in Figure 3(b). The computed results by modeling show the droplet diameters reduced by about 30% with increase in the voltage from 3 kV to 5 kV at the lowest flow rate, $\delta = 13.9$, in Figure 3(b).

Figure 4 shows distributions of the cone radius, R, and the charge density, ρ_E^* , along the meniscus for varying operating conditions and liquid properties about the reference condition, $\delta=13.9$, $V=4\,\mathrm{kV}$. ρ_E^* is the volumetric charge density nondimensionalized by $\frac{(\gamma\sigma\mathcal{Q})^{\frac{1}{2}}}{\pi d_1^2 v_s}$, where $v_s=\frac{\mathcal{Q}}{\pi d^2}$ is the scaling parameter for jet velocity ([7]). In Figure 4(a) the flow rate decreasing from $\delta=69.6$ to $\delta=13.9$ results in a steeper meniscus induced by increasing tangential electric field and increasing charge density according to the Gauss's law in Eq. 9. Note the electric field magnitude increasing exponentially as the flow rate decreases, as given in [30]. A high charge density leads to a high F_E in Eq. 12 resulting in a fine jet and small droplets with a short L_{cj} . Likewise, the increase in γ from 0.01 N m⁻¹ to $0.05\,\mathrm{N}\,\mathrm{m}^{-1}$ results in transition of the meniscus from a concave (towards vacuum) to a flattened shape. Note the largest $\rho_{E,max}$ and the shortest L_{cj} at the largest γ of $0.05\,\mathrm{N}\,\mathrm{m}^{-1}$ in Figure 4(b). In Figure 4(c), the tangential force increases with the increasing voltage up to $4.0\,\mathrm{kV}$ to result in a steeper meniscus leading to a finer jet and smaller droplet diameters. Note the menisci largely invariant with respect to the kinematic viscosity, ν , varying in the range from $6.3\times10^{-7}\,\mathrm{Pa}\,\mathrm{s}$ to $5.0\times10^{-5}\,\mathrm{Pa}\,\mathrm{s}$ in Figure 4(d). ρ_E^* also remains approximately the same, varying about 3% within the tested range of the kinematic viscosity. Note the largest viscosity, $\nu=5.0\times10^{-5}\,\mathrm{Pa}\,\mathrm{s}$, resulting in a jet elongated up to the location, $z=2\,\mathrm{\mu m}$.

B. Moderate Conductivity

Figure 5 is the setup and computed results for liquid volume fraction and electric field for TBP of moderate conductivity in [28]. It involves nozzle inner and outer diameters equal to 110 μ m and 230 μ m, the diameter of the extractor orifice equal to 0.8 mm, and the distance between emitter and extractor equal to 2.5 mm. Note the maximum electric field of about $9.1 \times 10^7 \text{ V m}^{-1}$ at the cone-to-jet region, which is well below the minimum electric field of $\sim 1 \times 10^9 \text{ V m}^{-1}$ required for ion emission ([29]).

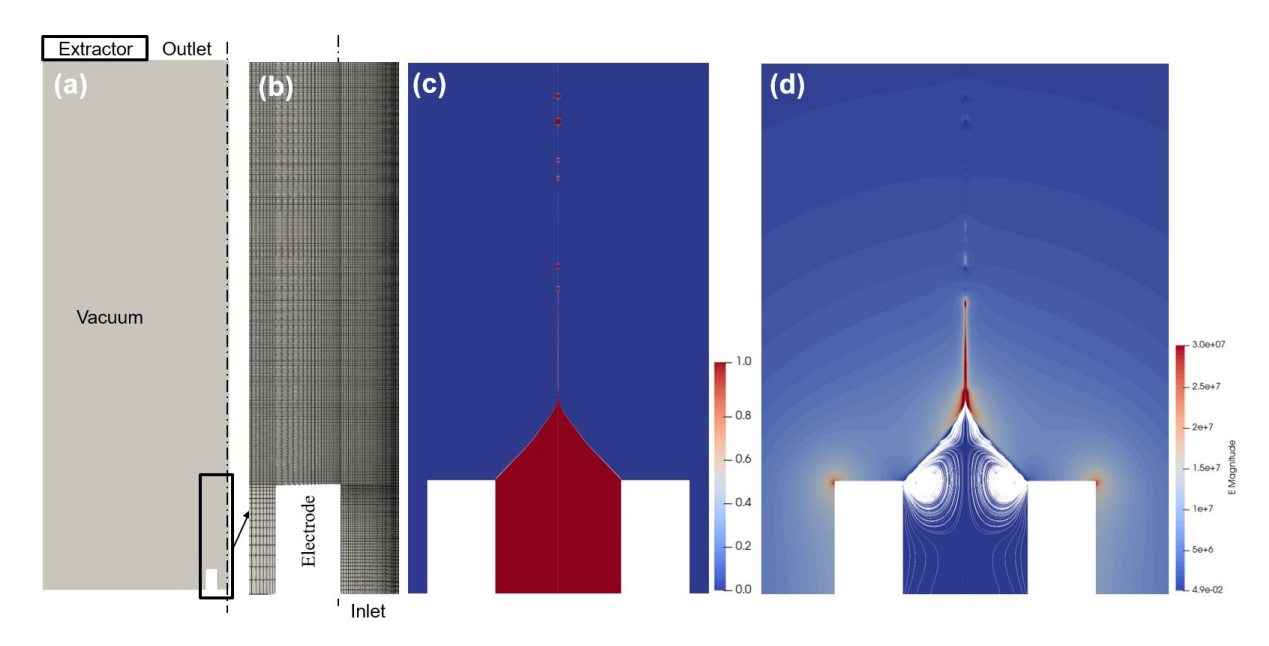


Fig. 5 Computation for TBP of moderate conductivity in steady cone-jet operation; (a) axisymmetric domain with 98,990 cells, (b) magnified emission region (c) liquid volume fraction and (d) magnitude of the electric field and the flow recirculation

Figure 5 shows the meniscus shape and the magnitude of the electric field in the steady cone-jet mode. Note the smaller jet diameter and smaller droplets together with smaller cone-to-jet length due to higher charge density and stronger electric field than those for heptane of lower conductivity in Figure 2.

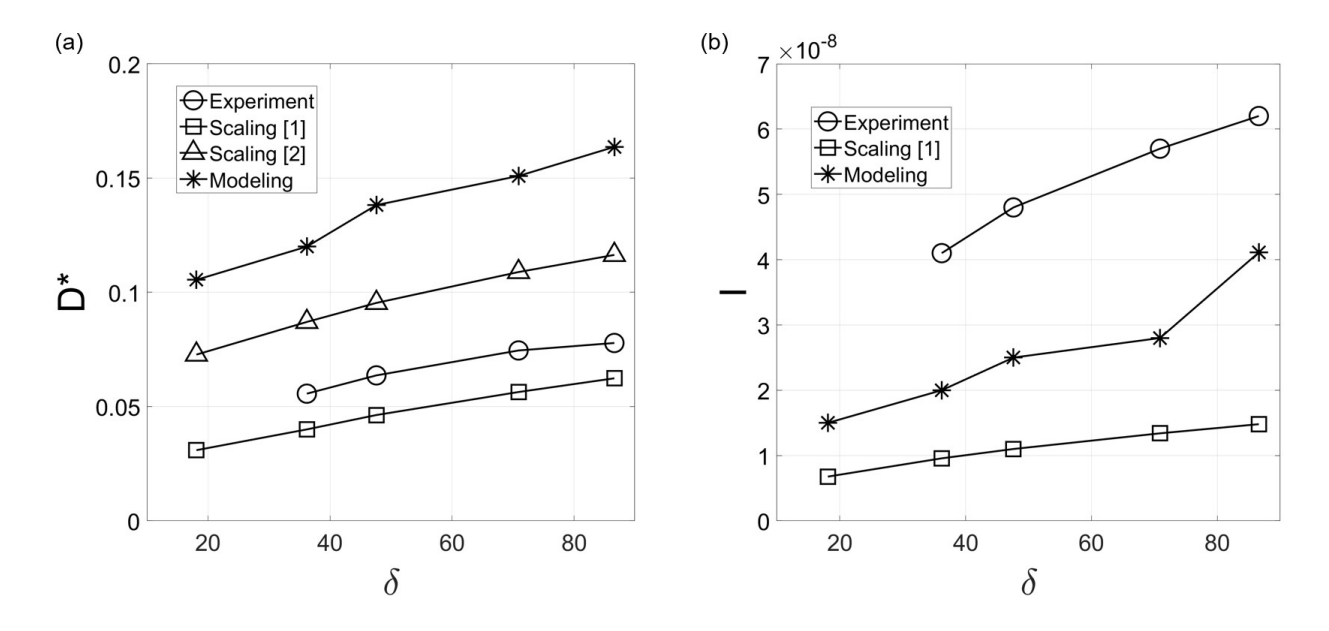


Fig. 6 Comparison of (a) dimensionless droplet diameters D^* , and (b) total currents I [A], by experiment ([28]), simulation and scaling by [6][1], [8][2] for TBP of moderate conductivity ($2.3 \times 10^{-4} \, \mathrm{S \, m^{-1}}$) with respect to varying δ for TBP of moderate conductivity ($\sigma = 2.3 \times 10^{-4} \, \mathrm{S \, m^{-1}}$)

Figure 6 shows the same trends of variation with reasonable quantitative agreement of droplet diameters and total currents by experiment, modeling and scaling laws in Eq. 19, 20, and 21. Deviation of the droplet diameters by

modeling may indicate numerical uncertainty or underpredicted electrostatic force due to ignoring viscous self-heating and temperature-dependent conductivity at a relatively low Reynolds number ([31, 32]). In experiment, droplets could fragment or undergo downstream influences such that droplets reaching the detector may not be those emitted off the jet ([33, 34]). Note in Figure 6(b) the total current by modeling lying between those by experiment ([28]) and scaling law proportional to half-power of the flow rate in Eq. 20.

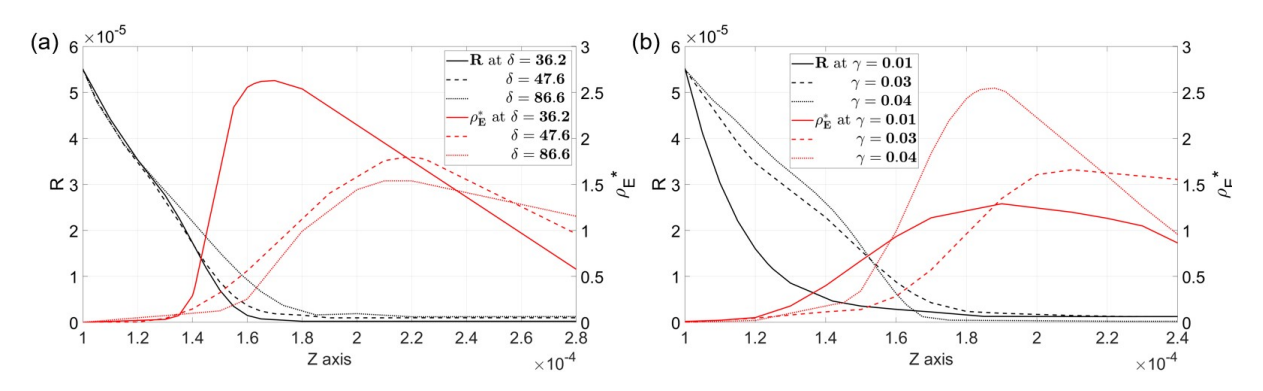


Fig. 7 Predicted distributions of radius and charge density distribution along the meniscus for TBP with respect to (a) δ , (b) γ [N m⁻¹], and (c) ε_r

Figure 7 shows the cone radius and the charge density along the meniscus for varying δ , γ , and ε_r about the reference condition, $\delta = 36.2$, V = 1.7 kV. Note a lower δ resulting in higher charge density so that the lowest $\delta = 36.2$ presents the highest ρ_E^* and the shortest L_{cj} in Figure 7(a). At a lower flow rate the jet may develop into an unstable whipping mode due to excessive electrostatic force as experimentally observed in [35]. Similarly, γ increasing from 0.01 N m⁻¹ to 0.04 N m⁻¹ results in increasing charge density with transition of the meniscus shape from concave to convex.

A scaling equation for the surface charge, q_s , was derived from a quasi-one-dimensional analytical model as ([36])

$$q_s = \varepsilon_0 E_0 = 0.62 \left(\varepsilon_0 \gamma^2 \rho \sigma^2 \right)^{\frac{1}{6}}.$$
 (22)

which supports ρ_E^* increasing with increasing γ in Figure 7(b). The change in ρ_E^* is associated with transition of the meniscus from convex-upward where $\frac{\partial^2 R}{\partial Z^2} = R'' < 0$ to concave-upward where R'' > 0. Note the maximum ρ_E^* for $\delta = 36.2$ or $\rho_E^* = 2.5$ for $\gamma = 0.07$ N m⁻¹ nearly doubled as compared with the maximum ρ_E^* without such transition for higher δ 's or lower γ 's, respectively. Rapid increase of ρ_E^* with a short L_{cj} after the inflection point suggests that charge accumulation takes place mostly in the concave-upward region where the electrostatic force dominates the surface tension and the viscous force for moderate to high conductivity liquids. Low δ or high γ results in high charge density associated with high electrostatic force, leading to steep menisci and smaller droplets. It is due to the geometrical constraint associated with transition of the meniscus from concave to convex according to the sign of the second-order derivative along the axis.

The cone-to-jet length was scaled as $\frac{\gamma}{\varepsilon_0 E_t^2} \sim \left(\frac{\varepsilon_0^2 \gamma}{\rho \sigma^2}\right)^{\frac{1}{3}} \delta$ in [6], where E_t is the tangential electric field. The predicted results are fitted as $L_{cj} \sim \delta^{0.42}$ for heptane and as $L_{cj} \sim \delta^{0.58}$ for TBP in Figure 8(a). Weaker dependence on δ for heptane is associated with lower charge density, resulting in a shorter L_{cj} than for TBP. Note lower $\rho_{E,max}$ at the cone-to-jet region for heptane than for TBP in Figure 8(a). The scaling, $L_{cj} \sim \delta^{0.58}$, fitted for TBP ($Re_E = 0.86$) shows stronger dependence than $L_{cj} \sim \delta^{0.17}$ from the BEM results in [10]. It is due to the emergence of convex meniscus leading to higher charge density and a shorter L_{cj} , which is not taken into account in [10]. In Figure 8(b), the specific charge of the emitted droplets decreases with increasing δ , to support the experimental observations for moderate conductivity ([28]). As a result, decreasing δ and increasing Re_E yields high charge concentration at the cone-to-jet region with shorter L_{cj} resulting in high specific charge (q/m) of the emitted droplets. Further work may be required to extend the new FVM to higher conductivity liquids, such as the ionic liquid, EMI-Im (1-Ethyl-3-methylimidazolium bis(trifluoromethylsulfonyl)imide) used in electric propulsion. The meniscus is expected to have a more convex conical shape ([35]) with an even shorter L_{cj} . The high normal electric field, E_n , due to increased charge density could explain possible ion evaporation at the high conductivity limit ([37–40]).

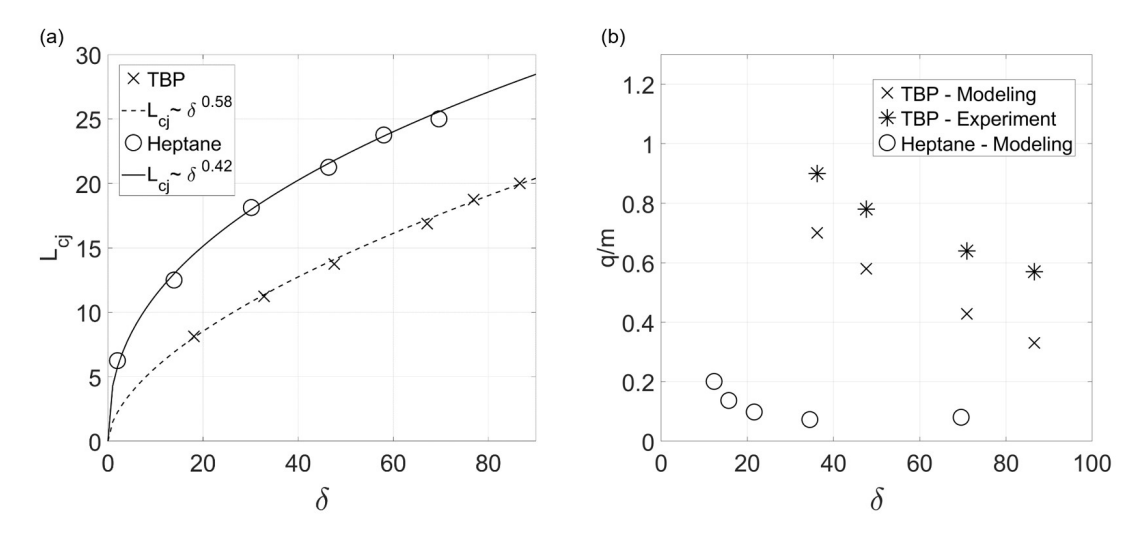


Fig. 8 Predicted (a) cone-to-jet length [μm] and (b) specific charge [C/kg] of the emitted droplet as a function of the non-dimensional flow rate, δ

V. Conclusion

We have developed an electrohydrodynamic model with finite volume analysis for low to moderate conductivity electrospray liquids. Compared to previous studies, this is the first Finite Volume Method (FVM) based model for higher conductivity liquid that accurately predicting the cone-jet formation and droplet breakup. This was possible by incorporating a novel interface interpolation devised to conserve the charge for higher conductivity. The model has been validated against experiments and scaling laws where measurements of specific charge, droplet diameters, and total current from the model show good agreement with experimental observations for both low and moderate conductivity liquids, such as heptane and tributyl phosphate. Although the initial conditions and resultant droplet measurements can be described with scaling laws, the emission mechanics during the evolution of a cone-jet are not described.

VI. Acknowledgements

This effort was supported by a grant from NASA's Jet Propulsion Laboratory, California Institute of Technology to support the LISA CMT development plan (NASA/JPL Award No. 1580267), the Air Force Research Lab at Edwards AFB, CA (Award No. 16-EPA-RQ-09), and Air Force Office of Scientific Research (AFOSR) (Award No. FA9550-21-1-0067). The authors would like to thank Adam Collins from UCLA; John Ziemer from NASA JPL; and David Bilyeu and Daniel Eckhardt from Air force Research Laboratory for their insightful discussions.

References

- [1] Zeleny, J., "The Electrical Discharge from Liquid Points, and a Hydrostatic Method of Measuring the Electric Intensity at Their Surfaces," *Phys. Rev.*, Vol. 3, 1914, pp. 69–91. https://doi.org/10.1103/PhysRev.3.69, URL https://link.aps.org/doi/10.1103/PhysRev.3.69.
- [2] Cloupeau, M., and Prunet-Foch, B., "Electrohydrodynamic spraying functioning modes: a critical review," *Journal of Aerosol Science*, Vol. 25, No. 6, 1994, pp. 1021–1036. https://doi.org/10.1016/0021-8502(94)90199-6.
- [3] Taylor, G. I., "Disintegration of water drops in an electric field," *Proceedings of the Royal Society of London. Series A. Mathematical and Physical Sciences*, Vol. 280, No. 1382, 1964, pp. 383–397. https://doi.org/10.1098/rspa.1964.0151, URL https://royalsocietypublishing.org/doi/abs/10.1098/rspa.1964.0151.
- [4] Melcher, J. R., and Taylor, G. I., "Electrohydrodynamics: A Review of the Role of Interfacial Shear Stresses," *Annual Review of Fluid Mechanics*, Vol. 1, No. 1, 1969, pp. 111–146. https://doi.org/10.1146/annurev.fl.01.010169.000551, URL https://doi.org/10.1146/annurev.fl.01.010169.000551.

- [5] Pantano, C., Gañán-Calvo, A., and Barrero, A., "Zeroth-order, electrohydrostatic solution for electrospraying in cone-jet mode," *Journal of Aerosol Science*, Vol. 25, No. 6, 1994, pp. 1065–1077. https://doi.org/https://doi.org/10.1016/0021-8502(94)90202-X, URL https://www.sciencedirect.com/science/article/pii/002185029490202X.
- [6] Gañán Calvo, A. M., "On the general scaling theory for electrospraying," *Journal of Fluid Mechanics*, Vol. 507, 2004, p. 203–212a. https://doi.org/10.1017/S0022112004008870.
- [7] Gañán-Calvo, A., Dávila, J., and Barrero, A., "Current and droplet size in the electrospraying of liquids. Scaling laws," *Journal of Aerosol Science*, Vol. 28, No. 2, 1997, pp. 249–275. https://doi.org/https://doi.org/10.1016/S0021-8502(96)00433-8, URL https://www.sciencedirect.com/science/article/pii/S0021850296004338.
- [8] De La Mora, J. F., and Loscertales, I. G., "The current emitted by highly conducting Taylor cones," *Journal of Fluid Mechanics*, Vol. 260, 1994, p. 155–184. https://doi.org/10.1017/S0022112094003472.
- [9] Higuera, F. J., "Flow rate and electric current emitted by a Taylor cone," *Journal of Fluid Mechanics*, Vol. 484, 2003, p. 303–327. https://doi.org/10.1017/S0022112003004385.
- [10] Gamero-Castaño, M., and Magnani, M., "Numerical simulation of electrospraying in the cone-jet mode," *Journal of Fluid Mechanics*, Vol. 859, 2019, p. 247–267. https://doi.org/10.1017/jfm.2018.832.
- [11] Roghair, I., Musterd, M., van den Ende, D., Kleijn, C., Kreutzer, M., and Mugele, F., "A numerical technique to simulate display pixels based on electrowetting," *Microfluidics and Nanofluidics*, Vol. 19, No. 2, 2015, pp. 465–482. https://doi.org/10.1007/s10404-015-1581-5.
- [12] Dastourani, H., Jahannama, M., and Eslami-Majd, A., "A physical insight into electrospray process in cone-jet mode: Role of operating parameters," *International Journal of Heat and Fluid Flow*, Vol. 70, 2018, pp. 315–335. https://doi.org/https://doi.org/10.1016/j.ijheatfluidflow.2018.02.012, URL https://www.sciencedirect.com/science/article/pii/S0142727X17310354.
- [13] López-Herrera, J., Popinet, S., and Herrada, M., "A charge-conservative approach for simulating electrohydrodynamic two-phase flows using volume-of-fluid," *J. Comput. Phys.*, Vol. 230, 2011, pp. 1939–1955.
- [14] Herrada, M. A., López-Herrera, J. M., Gañán Calvo, A. M., Vega, E. J., Montanero, J. M., and Popinet, S., "Numerical simulation of electrospray in the cone-jet mode," *Phys. Rev. E*, Vol. 86, 2012, p. 026305. https://doi.org/10.1103/PhysRevE.86.026305, URL https://link.aps.org/doi/10.1103/PhysRevE.86.026305.
- [15] Popinet, S., "Gerris: a tree-based adaptive solver for the incompressible Euler equations in complex geometries," *Journal of Computational Physics*, Vol. 190, No. 2, 2003, pp. 572–600. https://doi.org/https://doi.org/10.1016/S0021-9991(03)00298-5, URL https://www.sciencedirect.com/science/article/pii/S0021999103002985.
- [16] Tang, K., and Gomez, A., "Monodisperse Electrosprays of Low Electric Conductivity Liquids in the Cone-Jet Mode," *Journal of Colloid and Interface Science*, Vol. 184, No. 2, 1996, pp. 500–511. https://doi.org/https://doi.org/10.1006/jcis.1996.0645, URL https://www.sciencedirect.com/science/article/pii/S0021979796906451.
- [17] Brackbill, J., Kothe, D., and Zemach, C., "A continuum method for modeling surface tension," *Journal of Computational Physics*, Vol. 100, No. 2, 1992, pp. 335–354. https://doi.org/https://doi.org/10.1016/0021-9991(92)90240-Y, URL https://www.sciencedirect.com/science/article/pii/002199919290240Y.
- [18] Hirt, C., and Nichols, B., "Volume of fluid (VOF) method for the dynamics of free boundaries," *Journal of Computational Physics*, Vol. 39, No. 1, 1981, pp. 201–225. https://doi.org/https://doi.org/10.1016/0021-9991(81)90145-5, URL https://www.sciencedirect.com/science/article/pii/0021999181901455.
- [19] Rusche, H., "Computational fluid dynamics of dispersed two-phase flows at high phase fractions," 2003.
- [20] Aboukhedr, M., Georgoulas, A., Marengo, M., Gavaises, M., and Vogiatzaki, K., "Simulation of micro-flow dynamics at low capillary numbers using adaptive interface compression," *Computers and Fluids*, Vol. 165, 2018, pp. 13–32. https://doi.org/https://doi.org/10.1016/j.compfluid.2018.01.009, URL https://www.sciencedirect.com/science/article/pii/S0045793018300094.
- [21] Hoang, D. A., van Steijn, V., Portela, L. M., Kreutzer, M. T., and Kleijn, C. R., "Benchmark numerical simulations of segmented two-phase flows in microchannels using the Volume of Fluid method," *Computers and Fluids*, Vol. 86, 2013, pp. 28–36. https://doi.org/https://doi.org/10.1016/j.compfluid.2013.06.024, URL https://www.sciencedirect.com/science/article/pii/S0045793013002612.
- [22] Jasak, H., and Uroić, T., Practical Computational Fluid Dynamics with the Finite Volume Method, Springer International Publishing, Cham, 2020, pp. 103–161. https://doi.org/10.1007/978-3-030-37518-8_4, URL https://doi.org/10.1007/978-3-030-37518-8_4.

- [23] Okagaki, Y., Yonomoto, T., Ishigaki, M., and Hirose, Y., "Numerical Study on an Interface Compression Method for the Volume of Fluid Approach," *Fluids*, Vol. 6, No. 2, 2021. https://doi.org/10.3390/fluids6020080, URL https://www.mdpi.com/2311-5521/6/2/80.
- [24] Vaughan, N. D., Johnston, D. N., and Edge, K. A., "Numerical Simulation of Fluid Flow in Poppet Valves," *Proceedings of the Institution of Mechanical Engineers, Part C: Journal of Mechanical Engineering Science*, Vol. 206, No. 2, 1992, pp. 119–127.
- [25] Kothe, D., Rider, W., Mosso, S., Brock, J., and Hochstein, J., Volume tracking of interfaces having surface tension in two and three dimensions, 2012. https://doi.org/10.2514/6.1996-859, URL https://arc.aiaa.org/doi/abs/10.2514/6.1996-859.
- [26] Roenby, J., Bredmose, H., and Jasak, H., "A computational method for sharp interface advection," Royal Society Open Science, Vol. 3, No. 11, 2016, p. 160405. https://doi.org/10.1098/rsos.160405, URL https://royalsocietypublishing.org/doi/abs/10.1098/rsos.160405.
- [27] Tomar, G., Gerlach, D., Biswas, G., Alleborn, N., Sharma, A., Durst, F., Welch, S., and Delgado, A., "Two-phase electrohydrodynamic simulations using a volume-of-fluid approach," *Journal of Computational Physics*, Vol. 227, No. 2, 2007, pp. 1267–1285. https://doi.org/10.1016/j.jcp.2007.09.003, URL https://www.sciencedirect.com/science/article/pii/S0021999107003932.
- [28] Gamero-Castaño, M., and Hruby, V., "Electric measurements of charged sprays emitted by cone-jets," *Journal of Fluid Mechanics*, Vol. 459, 2002, p. 245–276. https://doi.org/10.1017/S002211200200798X.
- [29] Gamero-Castaño, M., "Electric-Field-Induced Ion Evaporation from Dielectric Liquid," *Phys. Rev. Lett.*, Vol. 89, 2002, p. 147602. https://doi.org/10.1103/PhysRevLett.89.147602, URL https://link.aps.org/doi/10.1103/PhysRevLett.89.147602.
- [30] Gamero-Castaño, M., "Electric-field-induced ion evaporation from dielectric liquid." Physical review letters, Vol. 89 14, 2002, p. 147602.
- [31] Vila, J., Ginés, P., Pico, J., Franjo, C., Jiménez, E., Varela, L., and Cabeza, O., "Temperature dependence of the electrical conductivity in EMIM-based ionic liquids: Evidence of Vogel–Tamman–Fulcher behavior," *Fluid Phase Equilibria*, Vol. 242, No. 2, 2006, pp. 141–146. https://doi.org/https://doi.org/10.1016/j.fluid.2006.01.022, URL https://www.sciencedirect.com/science/article/pii/S0378381206000793.
- [32] Gamero-Castaño, M., "Dissipation in cone-jet electrosprays and departure from isothermal operation." *Physical review. E*, Vol. 99 6-1, 2019, p. 061101.
- [33] Thuppul, A., Collins, A. L., Wright, P. L., Uchizono, N. M., and Wirz, R. E., "Mass flux and current density distributions of electrospray plumes," *Journal of Applied Physics*, Vol. 130, No. 10, 2021, p. 103301. https://doi.org/10.1063/5.0056761, URL https://doi.org/10.1063/5.0056761.
- [34] Ma, C., and Ryan, C., "Plume particle energy analysis of an ionic liquid electrospray ion source with high emission density," *Journal of Applied Physics*, Vol. 129, No. 8, 2021, p. 083302. https://doi.org/10.1063/5.0035889, URL https://doi.org/10.1063/5.0035889.
- [35] Uchizono, N. M., Collins, A. L., Thuppul, A., Wright, P. L., Eckhardt, D. Q., Ziemer, J., and Wirz, R. E., "Emission Modes in Electrospray Thrusters Operating with High Conductivity Ionic Liquids," *Aerospace*, Vol. 7, No. 10, 2020. https://doi.org/10.3390/aerospace7100141, URL https://www.mdpi.com/2226-4310/7/10/141.
- [36] Gañán Calvo, A. M., "THE SURFACE CHARGE IN ELECTROSPRAYING: ITS NATURE AND ITS UNIVERSAL SCALING LAWS," *Journal of Aerosol Science*, Vol. 30, No. 7, 1999, pp. 863–872. https://doi.org/https://doi.org/10.1016/S0021-8502(98)00780-0, URL https://www.sciencedirect.com/science/article/pii/S0021850298007800.
- [37] Miller, S. W., Prince, B. D., Bemish, R. J., and Rovey, J. L., "Electrospray of 1-Butyl-3-Methylimidazolium Dicyanamide Under Variable Flow Rate Operations," *Journal of Propulsion and Power*, Vol. 30, No. 6, 2014, pp. 1701–1710. https://doi.org/10.2514/1.B35170, URL https://doi.org/10.2514/1.B35170.
- [38] Gamero-Castaño, M., and Fernández de la Mora, J., "Direct measurement of ion evaporation kinetics from electrified liquid surfaces," *The Journal of Chemical Physics*, Vol. 113, No. 2, 2000, pp. 815–832. https://doi.org/10.1063/1.481857, URL https://doi.org/10.1063/1.481857.
- [39] Garoz, D., Bueno, C., Larriba, C., Castro, S., Romero-Sanz, I., Fernandez de la Mora, J., Yoshida, Y., and Saito, G., "Taylor cones of ionic liquids from capillary tubes as sources of pure ions: The role of surface tension and electrical conductivity," *Journal of Applied Physics*, Vol. 102, No. 6, 2007, p. 064913. https://doi.org/10.1063/1.2783769, URL https://doi.org/10.1063/1.2783769.

[40]	Romero-Sanz, I., Bocanegra, R., Fernandez de la Mora, J., and Gamero-Castaño, M., "Source of heavy molecular ions based on Taylor cones of ionic liquids operating in the pure ion evaporation regime," <i>Journal of Applied Physics</i> , Vol. 94, No. 5, 2003,
	pp. 3599–3605. https://doi.org/10.1063/1.1598281, URL https://doi.org/10.1063/1.1598281.